

# Detection of GeV $\gamma$ -Ray Emission from supernova remnant SNR G15.9+0.2 with Fermi-LAT

Yunchuan Xiang<sup>\*</sup>, Zejun Jiang<sup>†</sup> and Mengyao Tang

*Department of Astronomy, Key Laboratory of Astroparticle Physics of Yunnan Province, Yunnan University, Kunming 650091, China*

23 July 2021

## ABSTRACT

We first report GeV  $\gamma$ -ray emission from supernova remnant (SNR) G15.9+0.2 in this work. The results show that its power-law spectral index is  $2.94 \pm 0.25$  with a  $6.47\sigma$  significance level, and the  $\gamma$ -ray emission can be characterized by a two-dimensional (2D) Gaussian spatial distribution, which has a better improvement than the case of a point source. Moreover, we find that its likely counterparts from the radio, X-ray, and TeV energy bands are well coincident with its spatial location. Analyzing the variability from 12.4 years of the light curve (LC), we identify that this LC exists weak variability with a  $2.69\sigma$  variability significance level. We investigated the 2D Gaussian extended region and did not identify certified active galactic nuclei from the region of this SNR; thus, we suggest that the new  $\gamma$ -ray emission may originate from SNR G15.9+0.2. On this basis, we discussed the probable origins of its  $\gamma$ -ray radiation.

**Key words:** ISM: supernova remnants - gamma-rays: diffuse background - radiation mechanisms: non-thermal

arXiv:2103.07824v6 [astro-ph.HE] 21 Jul 2021

<sup>\*</sup> E-mail: xiang\_yunchuan@yeah.net

<sup>†</sup> E-mail: zjjiang@ynu.edu.cn

## 1 INTRODUCTION

SNR is considered to be an efficient cosmic-ray factory. After the explosion of SNR, it is considered that the 10% kinetic energy of SNR transferred to CRs, and the maximum energy of cosmic-ray particles can be accelerated to approximately  $10^{15}$  eV through the diffusive shock acceleration mechanism (Bell 1978; Blandford & Eichler 1987; Drury et al. 1994; Morlino & Caprioli 2012). Their multiband spectra exhibit a typical bimodal structure through leptonic or/and hadronic processes (e.g., Zeng et al. 2019, 2021). For the radio-to-X-ray band, it is generally recognized that synchrotron radiation dominates (Allen et al. 1997, 1999; Uchiyama et al. 2007). For the GeV-to-TeV energy band, inverse Compton scattering and bremsstrahlung of relativistic electrons are generally considered to be important mechanisms (Vink 2012). In addition, decay of neutral pions produced in the inelastic hadronic interaction becomes more and more important to explain the GeV and TeV emissions of SNRs (e.g., Xin et al. 2017, 2019; Yang et al. 2021; Xiang & Jiang 2021). Detection of GeV  $\gamma$ -ray emission of SNR is very important for evaluating SNR's contribution to cosmic-ray flux in Milky Way (Acero et al. 2016), and it can also help us explore the acceleration mechanism of cosmic-ray particles and limit the energy distribution of accelerated particles, which provides further understanding of the evolution process of cosmic-ray particles in SNRs (Zhang & Fang 2007; Finke & Dermer 2012; Tang et al. 2013). Thus far, only 24 SNRs have been firmly certified in the Fermi Large Telescope Fourth Source Catalog (4FGL; Abdollahi et al. 2020). Therefore, more GeV SNRs are required to recognize the nature of particle acceleration within SNRs.

For SNR G15.9+0.2, Clark et al. (1975) initially gave the result of the intensity gradient from the east region of the SNR, which is significantly higher than its west region, and its flux at 408 MHz is 7.7 Jy from Molonglo cross observations. At 5000 MHz, the flux is 1.4 Jy from the Parkes 64 m radio telescope, and its spectral index is -0.56. From the National Radio Astronomy Observatory (NRAO), Angerhofer et al. (1977) found a linear polarization distribution that was dominated by the background over SNR G15.9+0.2 at 4.9 GHz, and the peak value of the polarization distribution was 0.07 K. In addition, they presented a 5 GHz flux of  $\sim 1.1 \pm 0.2$  Jy with a spectral index of -0.63. Caswell et al. (1982) found a clear shell structure from SNR G15.9+0.2 at 1415 MHz with about  $58''$  resolution using the Fleurs synthesis radio telescope. Furthermore, they inferred a distance of 16.7 kpc, according to the relationship between the surface brightness and linear diameter and deduced its probable age of 3800 years. Based on the observations at 327.5 MHz and 1425 MHz from the NRAO VLA sky survey (NVSS), Dubner et al. (1996) found that the eastern border of SNR G15.9+0.2 had a bright shell feature; the northwest edge had two fainter knots; the north of the shell appeared an extension region of the radio emission with a  $3\sigma$  noise level at 1425 MHz.

Utilizing X-ray observations from Chandra, Reynolds et al. (2006) observed that the shell has a complete structure and a sharp feature from its outer edge. Moreover, from the integrated remnant spectrum of SNR G15.9+0.2, they found that the features with the strong  $K\alpha$  emission from Ca, Ar, S, Si, and Mg. Also, they estimated the age of SNR G15.9+0.2 at the order of  $10^3$  yr. Through XMM-Newton observations, Maggi & Acero (2017) found the evidence of spatial variations by measuring the Fe K line features. They believed that SNR G15.9+0.2 with the lowest Fe K centroid energy is the core-collapse SNR. Moreover, they identified ejecta emission from this SNR by observing the Fe K line features. They identified that the progenitors of SNR G15.9+0.2 originated from a massive star, according to the observation the abundance ratios of Ca, Ar, S, Si, and Mg.

For the GeV band data, Acero et al. (2016) did not find significant GeV  $\gamma$ -ray emission of the SNR in the 1-100 GeV energy band using the Fermi Large Area Telescope (Fermi-LAT), and they provided its upper limits with the 95% and 99% confidence level for the power-law spectral indices of 2.0 and 2.5, respectively. For the TeV energy band, H.E.S.S. Collaboration (2018) introduced the TeV source HESS J1818-1542. They provided an upper limit of the photon flux in the 1-10 TeV band, which is  $2.6 \times 10^{-13}$   $\text{cm}^{-2} \text{s}^{-1}$  with a  $3.7\sigma$  significance level. Although the distance between HESS J1818-1542 and SNR G015.9+00.2 is the closest than other TeV sources, there is a large angle separation with  $0^\circ.5$  between their positions. Therefore, their relevance is uncertain thus far. Abeysekara et al. (2017) found that the TeV source 2HWC J1819-150 is closer to SNR G15.9+0.2 with a position separation of  $0^\circ.1$ . In addition, the differential flux at 7 TeV is  $5.90 \pm 0.79 \times 10^{-15}$   $\text{TeV}^{-1} \text{cm}^{-2} \text{s}^{-1}$  with a spectral index of  $-2.88 \pm 0.10$ .

In this study, for the improvement and accumulation from the Fermi-LAT Pass 8 data and the update of  $\gamma$ -ray background models from galactic diffuse emission and the isotropic extragalactic emission (Abdollahi et al. 2020), the GeV  $\gamma$ -ray emission of SNR G15.9+0.2 was reanalyzed using approximately 12.4 years of the Pass 8 data. In the preliminary analysis, a likely GeV  $\gamma$ -ray emission from the region of SNR G15.9+0.2 was found, which strongly inspired us to explore the characteristics and origin of this GeV  $\gamma$ -ray emission in this study. Subsequent works include the introduction of data reduction in Section 2, the presentation of the analysis results in Section 3, and the discussion and conclusion about the likely origins of the GeV radiation in Section 4.

## 2 DATA REDUCTION

Using FermiTools version v11r5p3<sup>1</sup>, we analyzed the GeV  $\gamma$ -ray emission from the region of SNR G15.9+0.2 by selecting the instrumental response function (IRF) "P8R3\_SOURCE\_V3" and the Pass 8 "Source" event class (evtype = 3 and evclass = 128). The observation period was selected to be from August 4, 2008, to December 29, 2020 (mission elapsed time (MET) 239557427-630970757). The energy range was selected to be 1-500 GeV to reduce contamination from the galactic diffuse emission for a large point spread function in the low-energy band. Photon events with the maximum zenith angles of  $90^\circ$  were selected to suppress the pollution from the Earth Limb. A  $20^\circ \times 20^\circ$  region of

<sup>1</sup> <http://fermi.gsfc.nasa.gov/ssc/data/analysis/software/>

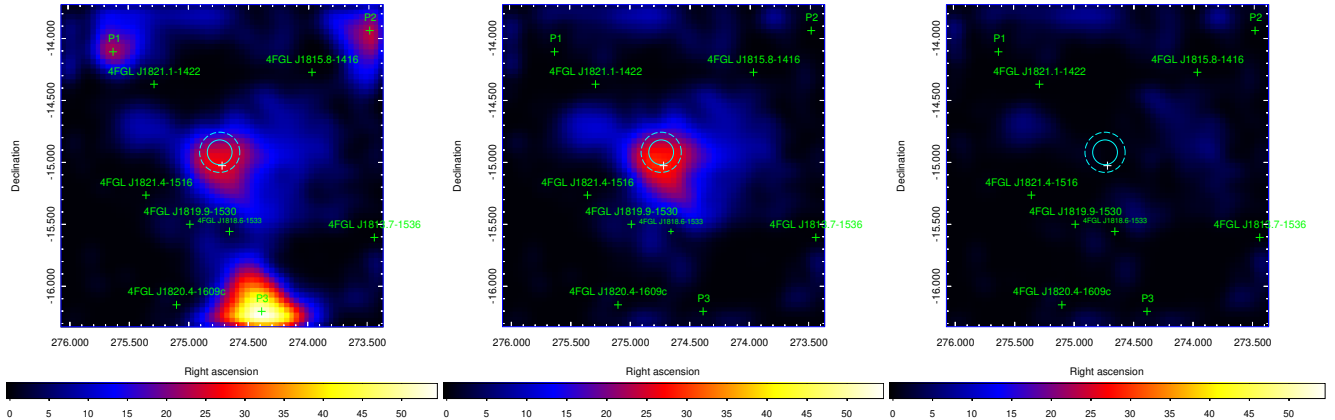


**Figure 1.** These TS maps of  $2^\circ.6 \times 2^\circ.6$ , which were smoothed with a Gaussian function with a kernel radius of  $0^\circ.3$ , in the 1-500 GeV energy band with a  $0^\circ.04$  pixel size centered at the SIMBAD position of SNR G15.9+0.2 marked as a white cross. The 68% and 95% error circles of the best-fit position of this SNR are marked by using solid and dashed cyan circles in these TS maps, respectively. Left panel: TS map including all the 4FGL sources and the residual radiations in the region. Middle panel: TS map after deducting three  $\gamma$ -ray excesses including P1-P3. Right panel: TS map after deducting all objects containing SNR G15.9+0.2 and adding three point sources.

interest (ROI), centered at the position from SIMBAD (R.A., decl.=  $274^\circ.72, -15^\circ.03$ )<sup>2</sup>, was selected for this analysis. We selected the script `make4FGLxml.py`<sup>3</sup> to generate a source model file, and sources from the 4FGL within the ROI of  $30^\circ$  were included in the model file. Then, we included a point source with a power-law spectrum at the SIMBAD location of SNR G15.9+0.2 to the model file. The binned likelihood tutorial<sup>4</sup> was followed in the analysis. Furthermore, spectral indexes and normalizations from sources within the  $5^\circ$  range of the ROI were set as free in the model file. The normalizations from the isotropic extragalactic emission (`iso_P8R3_SOURCE_V3_v1.txt`) and the galactic diffuse emission (`gll_iem_v07.fits`)<sup>5</sup> were also set as free.

### 3 SOURCE DETECTION

Running the command `gt tsmap`, the test statistic (TS) map, which is centered at the SIMBAD location of SNR G15.9+0.2 in the 1-500 GeV energy band, was first calculated in this analysis. In the left panel of Figure 1, significant  $\gamma$ -ray radiation with a TS value = 30.20 was found in the region of SNR G15.9+0.2. Here, the TS value, defined as  $TS = 2\log(L_1/L_0)$  from (Mattox et al. 1996), is calculated to quantify a significant source, and  $L_1$  and  $L_0$  represent maximum-likelihood values;  $L_1$  contains target source;  $L_0$  does not contain. In addition, we identified three significant  $\gamma$ -ray excesses from the locations of P1, P2, and P3. Then, we chose to add these three point sources, with power-law spectra in the local maxima of the TS map, to their locations<sup>6</sup> to subtract the three significant residual emissions within the  $2^\circ.6 \times 2^\circ.6$  TS map for all subsequent analyses. As shown in the middle panel of Figure 1, the  $\gamma$ -ray radiation was still significant with the TS value of 29.61 in the region of SNR G15.9+0.2.

To further confirm that the region of SNR G15.9+0.2 does not have other significant  $\gamma$ -ray residual radiations within the  $2^\circ.6 \times 2^\circ.6$  TS map, we also deducted the emission from the region of SNR G15.9+0.2. The results showed that there was no significant  $\gamma$ -ray excess from the region near SNR G15.9+0.2, as shown in the right panel of Figure 1, which suggests that the  $\gamma$ -ray emission is likely to come from SNR G15.9+0.2. Using `gt findsrc`, we obtained the best-fit position of SNR G15.9+0.2 to be (R.A., decl. =  $274^\circ.74, -14^\circ.92$ ) with a 68% (95%) error circle of  $0^\circ.10$  ( $0^\circ.16$ ) by assuming a point source with a power-law spectrum at its SIMBAD location. As shown in Figure 2, we found its contours of the 1.4 GHz radio and X-ray energy bands are all within the 68% and 95% error circles of the best position of SNR G15.9+0.2. Moreover, the region with a  $1\sigma$  statistical uncertainty from the location of the TeV source 2HWC J1819-150 (R.A., decl. =  $274^\circ.83, -15^\circ.06$ ; from Abeysekara et al. (2017) well overlaps with all the regions from three different energy bands. This indicates that these four sources from the radio to TeV bands are likely to be counterparts of SNR G15.9+0.2.

Using the uniform disk and two-dimensional (2D) Gaussian templates, we tested the different values of the radius and  $\sigma$ , which range from  $0^\circ.1$  to  $1^\circ.5$  with an increment of  $0^\circ.05$ , to obtain the probable  $\gamma$ -ray spatial distribution of the new source. Then, we calculated the value of the  $TS_{\text{ext}} \approx 26.06$ , using the formula of  $2\log(L_{\text{ext}}/L_{\text{ps}})$  from Lande et al. (2012), where  $L_{\text{ps}}$  and  $L_{\text{ext}}$  represent the maximum log-likelihood

<sup>2</sup> <http://simbad.u-strasbg.fr/simbad/>

<sup>3</sup> <https://fermi.gsfc.nasa.gov/ssc/data/analysis/user/>

<sup>4</sup> [https://fermi.gsfc.nasa.gov/ssc/data/analysis/scitools/binned\\_likelihood\\_tutorial.html](https://fermi.gsfc.nasa.gov/ssc/data/analysis/scitools/binned_likelihood_tutorial.html)

<sup>5</sup> <http://fermi.gsfc.nasa.gov/ssc/data/access/lat/BackgroundModels.html>

<sup>6</sup> The location of P1: (R.A., decl.= $275^\circ.63, -14^\circ.11$ ); that of P2: (R.A., decl.= $273^\circ.49, -13^\circ.99$ ); that of P3: (R.A., decl.= $274^\circ.39, -16^\circ.21$ ).

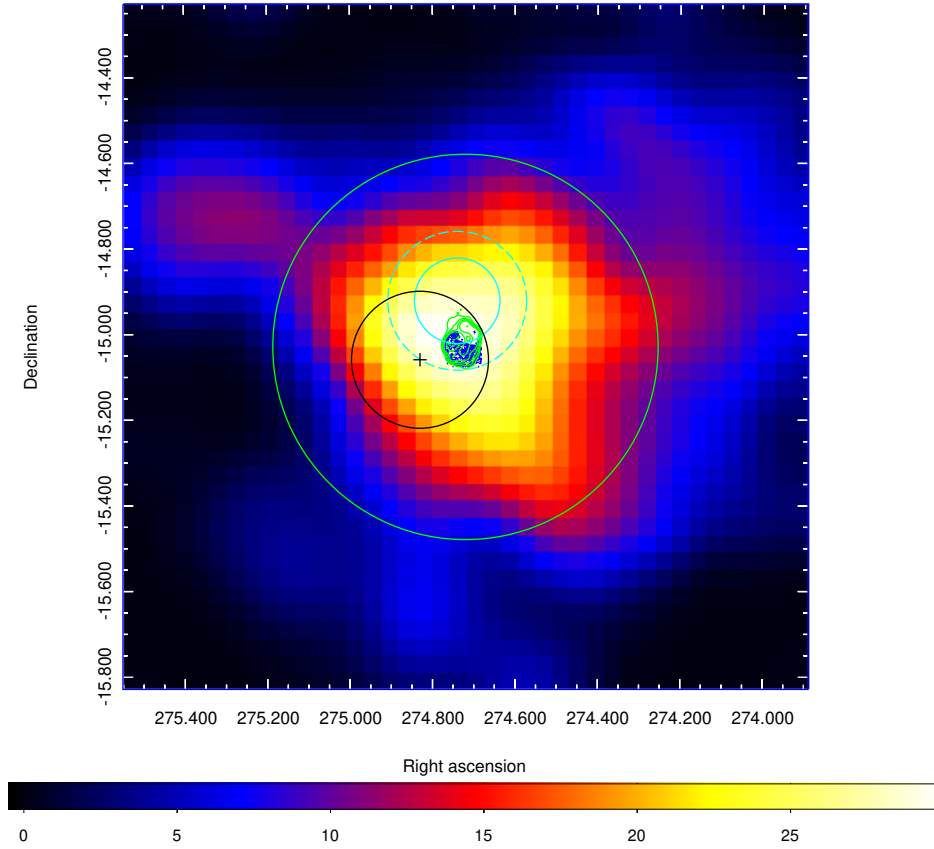


**Figure 2.** TS map of the region of  $1^\circ.6 \times 1^\circ.6$  is smoothed with a Gaussian kernel of  $0^\circ.3$  with a  $0^\circ.04$  pixel size in the 1-500 GeV energy band centered at the SIMBAD position of SNR G15.9+0.2. Two solid and dashed cyan circles were introduced in Figure 1. The green contours are from 1.4 GHz observations of NVSS (Caswell et al. 1982), and the blue contours are from X-ray observations of XMM-Newton (Maggi & Acero 2017). A black cross represents the position (RA=274°.83, decl.=−15°.06) of 2HWC J1819-150, and its  $1\sigma$  statistical uncertainty of this position is  $0^\circ.16$ , which is represented by a solid black circle (Abeysekara et al. 2017). The green circle indicate the extent of the GeV emission (2D Gaussian template) in this work.

**Table 1.** Spatial Distribution Analysis for SNR G15.9+0.2 with Different Spatial Models in The 1-500 GeV Energy Band

Spatial Model	Radius ( $\sigma$ ) degree	Spectral Index	Photon Flux $10^{-9}$ ph cm $^{-2}$ s $^{-1}$	TS Value	TS <sub>ext</sub>	Degrees of Freedom
Point source	-	2.94±0.51	0.39±0.10	29.61	-	4
2D Gaussian	$0^\circ.45$	2.94±0.25	4.09±0.57	55.67	26.06	5
uniform disk	$0^\circ.75$	2.96±0.23	3.62±0.53	50.93	21.32	5

values for the point source template and 2D Gaussian template with  $\sigma = 0^\circ.45$ , respectively. Considering a significant improvement with a high TS<sub>ext</sub>, compared with the case of a point source, we adopted the 2D Gaussian spatial template with a  $\sigma$  of  $0^\circ.45$  to analyze the new  $\gamma$ -ray source in all subsequent analyses. The best-fit results with the highest TS values from the different templates were presented in Table 1.

### 3.1 Spectral Analysis

In this analysis, we generated the spectral energy distribution (SED) in the 1-500 GeV energy band using a power-law spectrum model for the new  $\gamma$ -ray source. The SED was divided into 10 equal logarithmic bins. Each energy bin was fitted using the binned likelihood analysis method. For the energy bins with the TS value  $< 4$ , we calculated their upper limits with a 95% confidence level. Considering the subsequent energy bins with large statistical errors and the TS values  $< 4$ , here we selected to provide two upper limits for the SED, as shown in Figure 3.

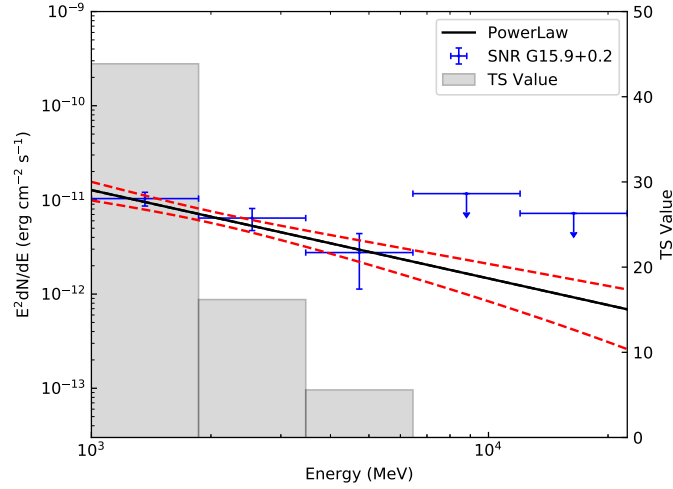


**Figure 3.** The SED of SNR G15.9+0.2 from the 1 GeV to 500 GeV energy band. Blue points indicate the result of the Fermi-LAT observation with the  $1\sigma$  statistical uncertainties. The black solid line represents the result of the global fit with a power-law spectral model, and the two red dashed lines represent the  $1\sigma$  statistical uncertainties of the global fit. The gray shaded areas represent the TS value of each energy bin. For the energy bins with TS values  $<4$ , the upper limits with a 95% confidence level are given.

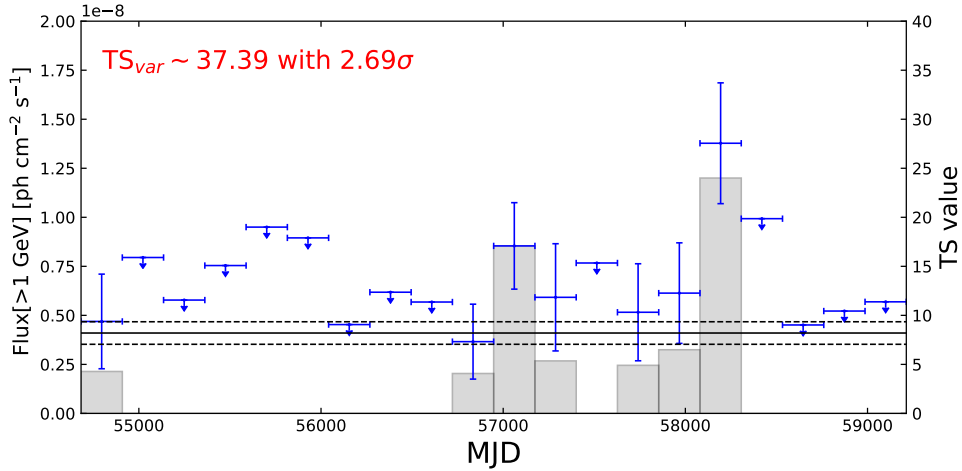


**Figure 4.** LC of SNR G15.9+0.2 with 20 time bins in the 1-500 GeV band. For the time bins with TS values  $<4$ , the upper limits with a 95% confidence level are given. The gray shaded areas show the TS value of each time bin. The black solid line and the two black dashed lines are used to show the average photon flux from the maximum likelihood fit and its  $1\sigma$  statistical uncertainties, respectively.

### 3.2 Variability Analysis

To check the variability of the photon flux over 12.41 years for the new  $\gamma$ -ray source, we generated a light curve (LC) with 20 time bins in the 1-500 GeV energy band, as can be seen from Figure 4. Calculating the variability index  $TS_{var}$  defined by Nolan et al. (2012), we acquired  $TS_{var} = 37.39$  with a  $2.69\sigma$  variability significance level. The result implies that the new  $\gamma$ -ray source exhibits weak variability<sup>7</sup>.

## 4 DISCUSSION AND CONCLUSION

By analyzing the above TS maps of SNR G15.9+0.2, we found that the region of SNR G15.9+0.2 has the significant GeV  $\gamma$ -ray radiation with a 2D Gaussian spatial distribution and a significance level of  $6.47\sigma$ . We observed that almost all the radio and X-ray contours from SNR

<sup>7</sup>  $TS_{var} \geq 36.19$  was used to identify variable sources at a 99% confidence level for the LC of 20 time bins (Xiang & Jiang 2021).

G15.9+0.2 are all within the  $2\sigma$  error circle. In addition, the  $1\sigma$  error circle also contains some contours from the radio and X-ray energy bands. These results suggest that the position of the new  $\gamma$ -ray source well coincides with SNR G15.9+0.2.

Next, we analyzed the variability of approximately 12.4 years of the LC and found that the LC exits a weak variability with a significance level of  $2.69\sigma$ . Thus far, the variability from LCs of SNRs in the Milky Way likely exists, such as iPTF14hls (Yuan et al. 2018), Supernova 2004dj (Xi et al. 2020; Ajello et al. 2020), the Crab Nebula (Arakawa et al. 2020). In addition, we investigated the 4FGL and found three certified SNRs with  $TS_{\text{var}} > 18.48^8$ , including W 51C, W 44, and IC 443, which implies the variability from the LC of SNR G15.9+0.2 is likely. We considered that the most significant GeV radiations of the region are concentrated in the 2D Gaussian region with  $0^\circ.45$  radius, as displayed in Figure 2, and the LC of the region has weak variability. Then, we used SIMBAD<sup>9</sup> and Aladin<sup>10</sup> to investigate whether the 2D Gaussian extended region has certified active galactic nuclei (AGN). However, we did not find likely one; therefore, we suggest that the new GeV  $\gamma$ -ray emission is more likely to be from SNR G15.9+0.2.

We considered leptonic and hadronic scenarios to explain the GeV SED of SNR G15.9+0.2 from this work using a one-zone model from NAIMA (Zabalza 2015, and references therein). Here we assumed leptonic and hadronic particle distributions satisfy  $N(E) = N_0 (E/E_0)^{-\alpha} \exp(-E/E_{\text{cutoff}})$ , where  $E_0$  is set to 1 TeV,  $N_0$  represents the amplitude,  $E$  is the particle energy,  $\alpha$  is the spectral index,  $E_{\text{cutoff}}$  represents the break energy (Aharonian et al. 2006; Xin et al. 2019; Xiang & Jiang 2021).

For the leptonic origin, the synchrotron radiation mechanism of leptons was originally used to explain the SED in the radio-to-X-ray energy band (e.g., Allen et al. 1997, 1999). The presence of very-high-energy (VHE) electrons are confirmed in SNRs (e.g., Tanimori et al. 1998), and the GeV and TeV emissions of SNRs are also observed (e.g., Ackermann et al. 2017; Abdalla et al. 2018a). To explain the SEDs of high-energy band from SNRs, inverse Compton scattering from leptons was widely used with the same particle distribution, which can also generate the radio-to-X-ray synchrotron spectrum (e.g., Tang et al. 2013; Condon et al. 2017; Zeng et al. 2017, 2019, 2021). Therefore, leptonic origin, as an important origin of high-energy emissions of SNRs, is considered in our analysis. Additionally, the detection of the characteristic pion-decay signature in IC 443 and W44 confirms that cosmic-ray protons can be accelerated in SNRs (Ackermann et al. 2013). The proportion of proton composition of the observed CR spectrum on Earth is 99%, suggesting that the hadronic contribution for the  $\gamma$ -ray emission from SNRs cannot be ignored (Liu et al. 2015). Recent studies have shown that the multi-band SED of certain SNRs can be better explained when considering the contribution of hadrons than a pure leptonic scenario. E.g., Puppis A (Xin et al. 2017), SNR G106.3+2.7 (Xin et al. 2019; Yang et al. 2021), Kepler's SNR (Xiang & Jiang 2021). Consequently, we also considered the hadronic origin here.

Subsequently, we investigated OH maser emission at 1720 MHz around SNR G15.9+0.2 (Green et al. 1997). However, we did not find the significant OH maser emission around SNR G15.9+0.2; thus, there is no convincing evidence to verify the interactions of SNR G15.9+0.2 with "OH" molecular clouds. Next, we investigated the CO high-resolution survey from Dempsey et al. (2013), as shown in Figure 5, we found denser molecular clouds in the  $1\sigma$  error circle of the best-fit position of SNR G15.9+0.2, which implies that this high-energy  $\gamma$ -ray radiation may originate from interactions between the target particles of the nearby CO molecular clouds (Wooten 1977; Denoyer 1979; Tatematsu et al. 1990; Arikawa et al. 1999; Reach & Rho 1999; Zhou et al. 2009; Kilpatrick et al. 2014). In addition, Tian et al. (2019) also proposed that the region of SNR G15.9+0.2 is likely to produce high-energy emissions, owing to the likely interactions between SNR G15.9+0.2 and the surrounding molecular clouds. In this case, we considered that a larger gas density may exist around SNR G15.9+0.2 than the upstream gas density  $n_{\text{gas}} = 0.7 \text{ cm}^{-3}$  at the shock from the SNR itself (Reynolds et al. 2006). Therefore, we also present the best-fit results of  $n_{\text{gas}} = 10 \text{ cm}^{-3}$  and  $100 \text{ cm}^{-3}$  in the panel (b) of Figure 6. Here, PYTHIA<sup>8</sup>, which involves the cross-section of proton-proton interactions and pion production from Kafexhiu et al. (2014), was selected to perform these analyses.

As observed in the two panels of Figure 6, leptonic and hadronic models with different gas densities can better explain the SED with a reduced  $\chi^2$  value of approximately 0.1 and 0.2, as shown in Table 2. In the future, additional observation data from different energy bands will be required to reveal the origin of the  $\gamma$ -ray emission from the region of SNR G15.9+0.2.

## ACKNOWLEDGMENT

We sincerely appreciate the support for this work from the National Key R&D Program of China under Grant No. 2018YFA0404204, the National Natural Science Foundation of China (NSFC U1931113, U1738211, 11303012), the Foundations of Yunnan Province (2018IC059, 2018FY001(-003), 2018FB011), the Scientific Research Fund of Yunnan Education Department (2020Y0039).

## DATA AVAILABILITY

The data underlying this work can be made available in Fermi Science Support Center<sup>11</sup> and will be shared on request to the corresponding author.

<sup>8</sup> The value of  $TS_{\text{var}} > 18.48$  over 12 intervals indicates that the source more than 99% chance is a variable source. Please refer <https://heasarc.gsfc.nasa.gov/W3Browse/fermi/fermilpsc.html>

<sup>9</sup> [simbad.u-strasbg.fr/simbad/](http://simbad.u-strasbg.fr/simbad/)

<sup>10</sup> <https://aladin.u-strasbg.fr/aladin.gml>

<sup>11</sup> <https://heasarc.gsfc.nasa.gov/FTP/fermi/data/lat/weekly/photon/>

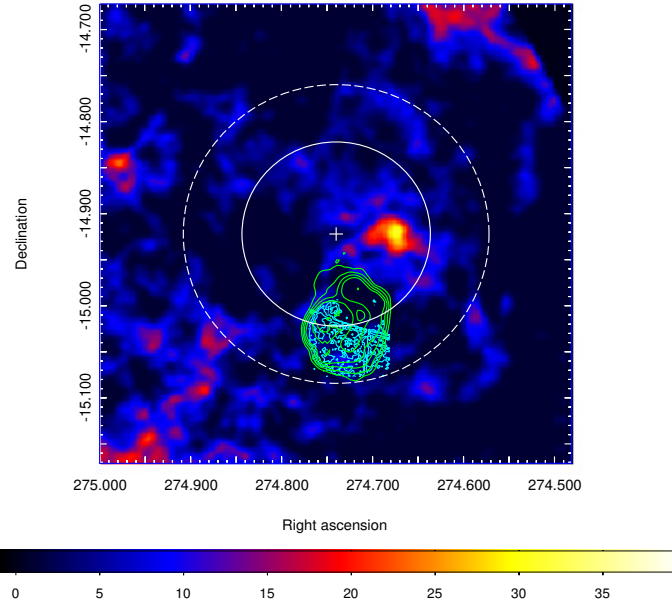


**Figure 5.** The  $0^{\circ}.5 \times 0^{\circ}.5$  velocity-integrated brightness temperature map, smoothed with a Gaussian kernel of  $0^{\circ}.3$ , from the CO Milky Way Survey (Dempsey et al. 2013). The color bar represents CO intensity with the units of  $\text{K km s}^{-1}$ . The 68% and 95% error circles of the best-fit position of this SNR are marked by using solid and dashed white circles in these TS maps, respectively. The green contours are from the observation of NVSS. The cyan contours are from the observation of XMM-Newton.

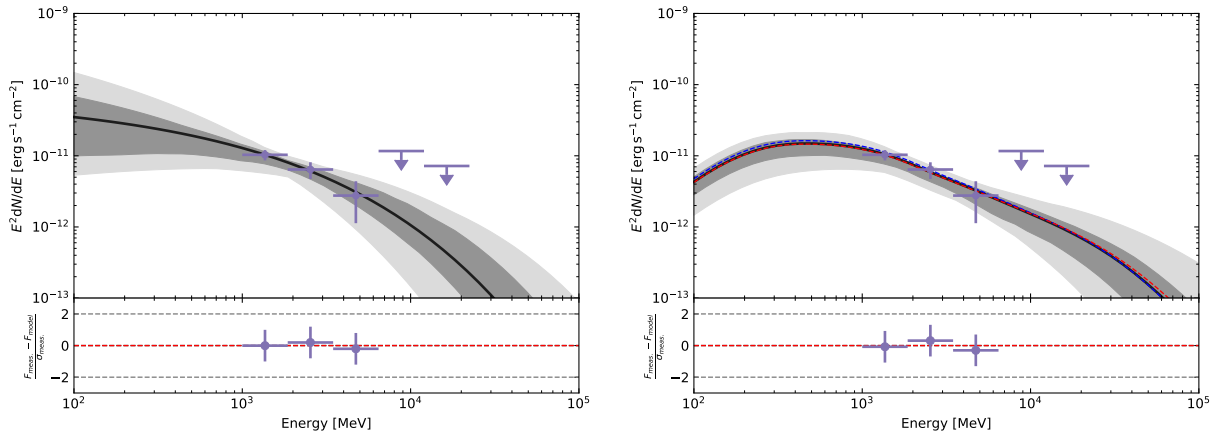


**Figure 6.** Left panel: the leptonic scenario that is dominated by the inverse Compton scattering, where the best-fit  $\gamma$ -ray spectrum is represented by using a black solid line. Right panel: the hadronic scenario that is dominated by the decay of neutral pions from the process of proton-proton interactions, where the best-fit results of  $n_{\text{gas}} = 0.7 \text{ cm}^{-3}$ ,  $n_{\text{gas}} = 10 \text{ cm}^{-3}$ , and  $n_{\text{gas}} = 100 \text{ cm}^{-3}$  are indicated by a black solid line, a blue dashed line, and a red dashed line, respectively. The  $1\sigma$  and  $3\sigma$  confidence intervals of the two panels are represented by the dark and light gray shaded regions, respectively. The best-fit residual maps are represented under these panels.

## REFERENCES

- Abeysekara A. U. et al., 2017, *APJ*, 843, 40  
 Abdalla H. et al., 2018a, *A&A*, 612, A1  
 Abdollahi S. et al., 2020, *ApJS*, 247, 33  
 Acero F. et al., 2016b, *ApJS*, 224, 8  
 Ackermann M. et al., 2013, *Sci*, 339, 807  
 Ackermann M. et al., 2017, *ApJ*, 843, 139  
 Aharonian F. et al., 2006, *A&A*, 449, 223

**Table 2.** The Best-fit Parameters of Leptonic and Hadronic Models

Model Name	$n_{\text{gas}}$ $\text{cm}^{-3}$	$\alpha$	$E_{\text{cutoff}}$ TeV	$W_e$ (or $W_p$ ) $10^{51}$ erg	$\chi^2/N_{\text{dof}}$
Leptonic model	—	$2.93^{+0.59}_{-0.63}$	$0.30^{+0.09}_{-0.07}$	$34.70^{+3.36}_{-3.13}$	$\frac{0.04 \pm 2}{5-4} = 0.08$
Hadronic model	0.7	$2.82^{+0.09}_{-0.10}$	$0.16^{+0.09}_{-0.07}$	$37.88^{+0.77}_{-0.80}$	$\frac{0.10 \pm 2}{5-4} = 0.20$
Hadronic model	10	$2.82^{+0.08}_{-0.14}$	$0.13^{+0.09}_{-0.08}$	$0.51^{+0.07}_{-0.06}$	$\frac{0.09 \pm 2}{5-4} = 0.18$
Hadronic model	100	$2.82^{+0.19}_{-0.14}$	$0.16^{+0.10}_{-0.10}$	$0.06^{+0.006}_{-0.008}$	$\frac{0.08 \pm 2}{5-4} = 0.16$

**Note:** For the distance of SNR G15.9+0.2, we took 8.5 kpc from [Reynolds et al. \(2006\)](#) for fitting the SED, and the energy band of the particles  $> 1$  GeV is selected to calculate the values of  $W_e$  and  $W_p$ .

- Ajello M., Di Mauro M., Paliya V. S., Garrappa S., 2020, *ApJ*, 894, 88  
Allen G. E. et al., 1997, *ApJ*, 487, L97  
Allen G.E., Gotthelf E.V., Petre, 1999, in *International Cosmic Ray Conference*, 3, 480  
Angerhofer P. E., Becker R. H., Kundu M. R., 1977, *A&A*, 55, 11  
Arakawa M., Hayashida M., Khangulyan D., Uchiyama Y., 2020, *ApJ*, 897, 33  
Arikawa Y., Tatematsu K., Sekimoto Y., Takahashi T., 1999, *PASJ*, 51, L7  
Bell A. R., 1978, *MNRAS*, 182, 147  
Blandford R., Eichler D., 1987, *PhR*, 154, 1  
Caswell J. L., Haynes R. F., Milne D. K., Wellington K. J., 1982, *MNRAS*, 200, 1143  
Clark D. H., Caswell J. L., Green A. J., 1975, *AuJPA*, 37, 1  
Condon B., Lemoine-Goumard M., Acero F., Katagiri H., 2017, *ApJ*, 851, 100  
Dempsey J. T., Thomas H. S., Currie M. J., 2013, *ApJS*, 209, 8  
Denoyer L. K., 1979a, *ApJL*, 232, L165  
Drury L. O., Aharonian F. A., Völk H. J., 1994, *A&A*, 287, 959  
Dubner G. M., Giacani E. B., Goss W. M., Moffett D. A., & Holdaway M., 1996, *AJ*, 111, 1304  
Finke J.D., Dermer C. D., 2012, *ApJ*, 751, 65  
Green A. J., Frail D. A., Goss W. M., Otrupcek R., 1997, *AJ*, 114, 2058  
H.E.S.S. Collaboration, 2018, *A&A*, 612, A3  
Kafexhiu E., Aharonian F., Taylor A. M., Vila G. S., 2014, *Phys. Rev.*, D90, 123014  
Kilpatrick C. D., Bieging J. H., Rieke G. H., 2014, *ApJ*, 796, 144  
Lande J. et al., 2012, *ApJ*, 756, 5  
Liu B. et al., 2015, *APJ*, 809, 102  
Maggi P., Acero F., 2017, *A&A*, 597, A65  
Mattox, J. R., Bertsch, D. L., Chiang, J. et al., 1996, *ApJ*, 461, 396  
Morlino G., Caprioli D., 2012, *AIPC*, 1505, 241  
Nolan P. L. et al., 2012, *ApJS*, 199, 31  
Reach W. T., Rho J., 1999, *ApJ*, 511, 836  
Reynolds S. P. et al., 2006, *ApJ*, 652, L45  
Tang Y.Y., Dai Z.C., Zhang L., 2013, *RAA*, 13, 537  
Tanimori T. et al., 1998, *APJ*, 497, L25  
Tatematsu K., Fukui Y., Iwata T., Seward F. D., Nakano M., 1990, *ApJ*, 351, 157  
Tian W. W. et al., 2019, *PASP*, 131, 114301  
Uchiyama Y., Aharonian F. A., Tanaka T., Takahashi T., Maeda Y., 2007, *Nature*, 449, 576  
Vink J., 2012, *A&ARv*, 20, 49  
Wootten H. A., 1977, *ApJ*, 216, 440  
Xi S.Q. et al., 2020, *APJ*, 901, 158  
Xiang Y.C., Jiang Z.J., 2021, *APJ*, 908, 22  
Xin Y.L. et al., 2017, 843,90  
Xin Y.L., Zeng H.D., Liu S.M., Fan Y.Z., Wei D.M., 2019, *ApJ*, 885, 162  
Yang C.Y., Zeng H.D., Bao B.W., Zhang L., 2021, preprint (arXiv:2106.02629)  
Yuan Q. et al., 2018, *ApJL*, 854, L18  
Zabalza V., 2015, preprint (arXiv:1509.03319)  
Zeng H. et al., 2017, *ApJ*, 834, 153  
Zeng H., Xin Y., Liu S., 2019, *ApJ*, 874, 50  
Zeng H.D., Xin Y.L., Zhang S.N., Liu S.M., 2021, *ApJ*, 910, 78  
Zhang L., Fang J., 2007, *ApJ*, 666, 247  
Zhou X., Chen Y., Su Y., Yang J., 2009, *ApJ*, 691, 516